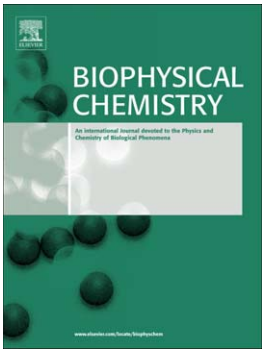


# Evidence of lipid peroxidation and protein phosphorylation in cells upon oxidative stress photo-generated by fullerols

B. Vileno, S. Jeney, A. Sienkiewicz, P.R. Marcoux, L.M. Miller, L. Forró

PII: S0301-4622(10)00228-0
DOI: doi: 10.1016/j.bpc.2010.09.004
Reference: BIOCHE 5430

To appear in: *Biophysical Chemistry*

Received date: 26 July 2010
Revised date: 18 September 2010
Accepted date: 18 September 2010

Please cite this article as: B. Vileno, S. Jeney, A. Sienkiewicz, P.R. Marcoux, L.M. Miller, L. Forró, Evidence of lipid peroxidation and protein phosphorylation in cells upon oxidative stress photo-generated by fullerols, *Biophysical Chemistry* (2010), doi: 10.1016/j.bpc.2010.09.004

# Evidence of lipid peroxidation and protein phosphorylation in cells upon oxidative stress photo-generated by fullerols

B. Vileno[1,*], S. Jeney[1],A. Sienkiewicz[1], P.R. Marcoux[2], L.M. Miller[3], L. Forró[3]

*[1]NN Group, Institute of Physics of Condensed Matter, School of Basic Sciences (Station 3), Swiss Federal Institute of Technology (EPFL), CH-1015 Lausanne. [2]LETI / DTBS / Equipe commune CEA – bioMérieux CEA, 17 rue des Martyrs 38054 Grenoble cedex 9 France. [3] National Synchrotron Light Source, Brookhaven National Laboratory, Upton, NY 11973. *Present address: POMAM Lab. Institut de Chimie de Strasbourg, UMR7177 - CNRS-UDS. 1,rue Blaise Pascal, BP296/R8, 67008 Strasbourg FRANCE. e-mail: vileno@unistra.fr*



## ABSTRACT

An Oxidative Stress (OS) state is characterized by the generation of Reactive Oxygen Species (ROS) in a biological system above its capacity to counterbalance them [1]. Exposure to OS induces the accumulation of intracellular ROS, which in turn causes cell damage in the form of protein, lipid, and/or DNA oxidations. Such conditions are believed to be linked to numerous diseases or simply to the ageing of tissues. However, the controlled generation of ROS *via* photosensitizing drugs or photosensitizers (PS) is now widely used to treat various tumors and other infections [2,3]. Here we present a method to track the chemical changes in a cell after

exposure to oxidative stress. OS is induced *via* fullerols, a custom made water soluble derivative of fullerene ($C_{60}$), under visible light illumination. Synchrotron-based Fourier Transform InfraRed Microspectroscopy (S-FTIRM) was used to assess the chemical makeup of single cells after OS exposure. Consequently, a chemical fingerprint of oxidative stress was probed in this study through an increase in the bands linked with lipid peroxidation (carbonyl ester group at 1740 $cm^{-1}$) and protein phosphorylation (asymmetric phosphate stretching at 1240 $cm^{-1}$).

**KEYWORDS:**

IR, Infrared Spectroscopic Microscopy, Synchrotron, Fullerols, Reactive Oxygen Species, Oxidative Stress

**RUNNING TITLE:** Oxidative Stress on living cells studied by FTIRM.

**MAIN TEXT**

**INTRODUCTION:**

Reactive oxygen species (ROS) are important intermediates in photo-oxidative processes. ROS include non-exhaustively, hydroxyl radical ($OH^{\bullet}$), superoxide anion ($O_2^{\bullet -}$), electronically-excited di-oxygen, *i.e.* singlet oxygen ($^1\Delta_g$), peroxynitrite ($ONOO^{\bullet -}$) and hydrogen peroxide ($H_2O_2$). If ROS play important roles in living systems, both as key intermediates in physiological processes and as strong oxidants, they are also responsible for the oxidative stress (OS) underlying various deleterious processes. In living cells, OS occurs when enhanced ROS generation exceeds the basal level of cellular protective mechanisms. The cells are then damaged by oxidization of their subcellular components, which can lead to cell apoptosis or necrosis. In

particular, elevated ROS levels in cells are associated with the aging process [4], as well as with many pathological disease processes [1,5]. Among various ROS involved in bio-oxidative and bio-photo-oxidative processes, $^1\Delta_g$ plays a significant role. In particular, $^1\Delta_g$ is involved in light-induced photo-damage to the eyes and skin [6]. $^1\Delta_g$ is known to be almost as reactive as atomic oxygen and to react directly with proteins and unsaturated lipids located in the cytosol and cell membranes to give the corresponding peroxides. Consequently, cell apoptosis, bacterial and viral inactivation are identified effects of $^1\Delta_g$ action [7,8] with higher yields than hydroxide ($OH^{\bullet}$) or superoxide ($O_2^{\bullet -}$) radicals [9].

Pristine fullerene ($C_{60}$), due to its unique electronic $\pi$-system, can generate $^1\Delta_g$ and other ROS in organic solvents under UV or visible light illumination [10]. It has also been shown that the poly-hydroxylated and highly water-soluble derivatives of $C_{60}$, also known as fullerols, are potent photosensitizers of ROS. In particular, evidence of generation of superoxide radicals via the so-called Type I mechanism, as well as $^1\Delta_g$ via an effective resonant energy transfer (Type I photosensitization pathway) was demonstrated for fullerol $C_{60}(OH)_{24}$ [11]. In a previous studywe have shown that a custom-synthesized fullerol ($C_{60}(OH)_{19}(ONa)_{17},18H_2O$) can efficiently generate $^1\Delta_g$ in aqueous milieus under visible light illumination and also pointed to a strong photo-toxicity of this compound towards cells [12] and cell compounds [13].

In this work, the oxidative stress on living monkey fibroblasts was mediated *via* ROS, which was photo-sensitized in the presence of the above–mentioned fullerol $C_{60}(OH)_{19}(ONa)_{17},18H_2O$ [12]. First, the generation of $^1\Delta_g$ by this water-soluble derivative of $C_{60}$ *via* Type II photodynamic process was confirmed in a cell-free EPR experiment using a $^1\Delta_g$ selective substrate, 2,2,6,6-

tetramethyl-4-piperidinol (TMP-OH). Then, the OS-induced biochemical alterations in living fibroblasts were tracked by Fourier Transform InfraRed Microspectroscopy (FTIRM) at the single cell level. To achieve the required subcellular spatial resolution, an IR beam size smaller than the cell size itself is needed. However, existing IRMS instruments using a conventional thermal (globar) source, encounter a Signal-to-Noise ratio (S/N) limitation when apertures confine the IR to an area of below 30 $\mu m^2$ [14]. Hence, for single cell imaging, the InfraRed (IR) synchrotron source delivers the entire infrared wavelength at much higher brightness than a globar source [15]. For a 10 by 10 $\mu m^2$ aperture, the S/N ratio is improved by a few orders of magnitude compared to globar sources [16]. In order to account for heterogeneities in living matter, we also looked for spectral anomalies for a given functional group in a population of at least 75 cells, allowing statistical sampling.

**MATERIALS AND METHODS:**

**Fullerol synthesis and ROS generation.** The fullerol synthesis was adapted from Chiang et al. [17], based on the oxidation of $C_{60}$ under strongly acidic conditions. The synthesis and characterization is detailed in [12]. The final stoichiometry used here was $C_{60}(OH)_{19}(ONa)_{17}$,$18H_2O$. White light illumination of an aqueous solution of fullerol leads to ROS generation. Depending on experimental conditions, either oxygen based radicals ($OH^{\bullet}$, $O_2^{\bullet}$) are generated via charge transfer (Type I pathway) or $^1\Delta_g$ following a resonant energy transfer pathway (Type II) [18]. Throughout all experiments, a 500 μM solution of fullerol in Phosphate Buffered Saline (PBS, pH = 7.4, Sigma), saturated with oxygen gas by bubbling for at

least 30 min, was used. All solutions were prepared with ultrapure water (18.2 MΩcm$^{-1}$; Milli-Q purification system, Millipore).

**ROS detection.** To confirm the generation of $^1\Delta_g$, we employed Electron Paramagnetic Resonance (EPR) in conjunction with reactive scavenging of $^1\Delta_g$ with a diamagnetic substrate, 2,2,6,6-tetramethyl-4-piperidinol (TMP-OH, Sigma). This approach, introduced firstly by Lion et al. [19], is now customarily considered as a highly specific technique for the detection of $^1\Delta_g$ in aqueous media [20]. The formation of a stable paramagnetic N-oxyl radical, 4-hydroxy-2,2,6,6,-tetramethyl-piperidineN-oxyl (TEMPOL) is monitored by EPR, resulting from the attack of $^1\Delta_g$ on TMP-OH. The unpaired electron in TEMPOL is primarily located in the $\pi$-orbital of the nitrogen $^{14}$N atom, which has a nuclear spin $\boldsymbol{I}$ =1. This gives rise to a characteristic EPR spectrum consisting of three equidistant and approximately equi-intense hyperfine features ($\boldsymbol{A}_N$ =1.69 mT, $\boldsymbol{g}$=2.0066, $\Delta H_{pp}$ = 0.158 mT). The EPR reactive scavenging of $^1\Delta_g$ is summarized in Figure 1a. The aqueous PBS solution (pH~7.4) containing 500 μM of fullerol was supplemented with TMP-OH at 50 mM. Prior to the EPR measurements, the oxygen saturated solutions were directly transferred into thin quartz capillaries (0.6/0.87 mm inner/outer diameter, with a sample height of 25 mm, VitroCom, NJ, USA) and sealed on both ends with Cha-Seal$^{TM}$ tube sealing compound (Medex International, Inc., USA). Solutions were then exposed to illumination with the white light from a spot light source (150W halogen lamp, Model 6000, Intralux, Switzerland). Immediately after exposure to visible light, the sample-holding capillaries were transferred into the EPR cavity of the EPR spectrometer (Model ESP300E from Bruker BioSpin GmbH). All the EPR experiments were carried out at room temperature. EPR spectra were

acquired in a conventional field-swept mode. Routinely, for each experimental point, ten-scan field-swept EPR spectra were recorded. The typical instrumental settings were: microwave frequency 9.38 GHz, microwave power 2.0 mW, sweep width 100 G, modulation frequency 100 kHz, modulation amplitude 1 G, receiver gain $1\times10^5$, time constant 20.48 ms, conversion time 40.96 ms, and time per single scan 41.9 s.

**Cell culture.** The monkey Fibroblast cell line COS-7 was cultured in Dulbecco's Modified Eagle Medium (DMEM, pH 7.4, Sigma) supplemented with 10% Fetal Calf Serum and 2 mM L-Glutamine. Cells were grown at 37°C, 95% air/ 5% $CO_2$, on non-coated Calcium fluoride ($CaF_2$) windows (13 mm diameter, 1 mm thickness, Crystran, UK) using an identical number of passages. $CaF_2$ is known to be non toxic to cells and fully transparent in the relevant IR range between 1000 and 4000 $cm^{-1}$. A density of 25000-30000 cells per window was deposited, and used for experiment before they reached confluent state (day 2–3), thus single cells were still distinguishable [21].

**Protocol of Cell Irradiations.** The cell–covered $CaF_2$–windows were removed from the culture medium, rinsed in PBS, placed in the photosensitizing solution (*i.e.* PBS supplemented by 500 μM $C_{60}(OH)_{19}(ONa)_{17}$), and then illuminated for three different exposure times (10, 20 and 30 min). Special care was taken not to heat the sample by the light source (Halogen Philips, 150W). After exposure, the photosensitizing solution was removed, the cells were rinsed in PBS, incubated for 30 min in DMEM, rinsed again with PBS and left to dry at 4°C under a soft air flow. Once fully dried, the windows were carefully re-washed with distilled water in order to

remove PBS salt crystals on the window surface, fully dried again and kept at 4°C until SIRMS experiments [22,23,24].

A Trypan Blue (TB, Sigma Aldrich) assay was used to probe the viability of the cells upon OS. TB is negatively charged and typically does not penetrate a cell unless its membrane is damaged. Consequently, all cells including this dye and thus having a blue stained cytoplasm are dead. Inversely all viable cells exclude the dye and have a clear cytoplasm. Noteworthy, the TB assay cannot differentiate between a necrotic or apoptotic cell.

**Synchrotron Infrared MicroSpectroscopy.** Synchrotron-based Fourier Transform Infrared Microspectroscopy (S-FTIRM) measurements were performed on dried cells prepared as described above. The S-FTIRM set-up [14] consists of a Thermo Nicolet Continum IR microscope coupled to a Thermo Nicolet Magna 860 FTIR (Thermo Nicolet Instrument, Madison, WI). An automated X-Y mapping stage allowed sample scanning with a step accuracy of 1 μm. The IR beam, with an aperture of 7 x 7 to 10 x 10 $\mu m^2$, was positioned on the center of a single flat cell chosen by conventional optical microscopy, illuminating most of the cell. Spectra were collected in transmission mode, at a spectral resolution of 4 $cm^{-1}$, and 128 to 256 scans were co-added to enhance the S/N ratio. Prior to each experiment, a background spectrum was taken at a clean cell-free place on the $CaF_2$ window and subtracted from the one with the sample. Data were analyzed using Omnic 7.4 (Thermo Fisher Scientific Inc), and Transform (Fortner Software). Few bad pixels were removed and replaced either by the mean value of their neighbor's pixel (e.g. for odd absorbance values) or set to zero (for negative values). It is worth noting that despite the high brightness of the IR source, the total energy delivered to a sample for

an aperture of 10 by 10 $\mu m^2$ is less than 5 mW [25]. The local rise of temperature under IR synchrotron irradiation has been determined to be lower than one degree [26]. Therefore, we assumed that heating had no effect on our experiment.

## RESULTS

**Kinetics of ROS-generation by $C_{60}(OH)_{19}(ONa)_{17}$.** The EPR measurements confirmed the photosensitization of $^1\Delta_g$ in PBS buffered $H_2O$ solutions in the presence of fullerol $C_{60}(OH)_{19}(ONa)_{17}$,18 $H_2O$. The typical EPR results on reactive scavenging of $^1\Delta_g$ are shown in Figure 1b. As shown in the inset, the observed EPR spectra are 1:1:1 triplets, indicative of TEMPOL, the paramagnetic product of the $^1\Delta_g$ attack on TMP-OH. The amplitude of the characteristic EPR signal of TEMPOL increased linearly until 20 min of illumination, pointing to a marked process of $^1\Delta_g$ -formation *via* Type II energy transfer from the light-excited triplet states of fullerols to the ground state triplets of dioxygen molecules.

**Cell viability under photo-oxidative stress.** As a preliminary study, a cell viability test was performed using a Trypan Blue dye exclusion assay. Cells were incubated after different exposure times to OS in solutions of 0.01 % TB in PBS. The buffer was then exchanged with pure PBS and cells were dried as described above. A significant increase of TB stained cells was observed after only 5 minutes of exposure to the combined effects of light and fullerol. The percentage of dead cells increased above 75% after 20 min of OS exposure. Control experiments suggested that neither the lone presence of the photosensitizer in the dark, nor the visible light illumination in the absence of PS, had a detectable effect on cell viability (TB stained cells <4%).

**Spectral IR signature.** As individual biochemical components have their specific vibrational fingerprints (see reference [27]), the various organic molecules present in a single cell shape an IRMS spectrum with complex overlapping absorption bands. Hence, one band can be associated with several compounds. A typical SIRMS spectrum of a single dried, non-treated fibroblast is shown in Figure 2 (top spectrum). The main spectral features observed in the cell with their associated characteristic functional groups were the following:

*(i)* The wide 3300 $cm^{-1}$ band (gray arrow) originates from both the N–H and O–H bonds present in water traces, polysaccharides, carbohydrates and proteins [28].

*(ii)* The band in the 2995-2800 $cm^{-1}$ region (green arrow) arises from the symmetric and asymmetric stretching modes of the carbon – hydrogen bond in methylene ($CH_2$) and methyl ($CH_3$) group mainly present in lipids and protein [29].

*(iii)*Between 1740 and 1725 $cm^{-1}$ (blue arrow) the shoulder is attributed to the contributions of the carbonyl ester group (>C=O) in non-hydrogen bonded and hydrogen-bonded states respectively, found in phospholipids [30].

*(iv)* The two absorption bands centered around 1650 and 1545 $cm^{-1}$ correspond to the intensity of Amide I (orange arrow) and Amide II (dashed gray arrow), respectively. Amide I originate from the C=O hydrogen bonded stretching vibrations. The Amide II peak, is also representative of a protein-based structure, and arises from C-N stretching and C-NH bending vibrations [31,32].

*(v)* The bands centered around 1235 $cm^{-1}$ and 1085 $cm^{-1}$ originate mainly from asymmetric phosphate ($asPO_2^-$, red arrow) and symmetric phosphate ($sPO_2^-$, dotted red arrow) stretching vibrations, respectively. They are attributed to the phosphodiester groups of nucleic acids from DNA. These two bands are also attributed to the C-O-P stretching modes present in phosphorylated lipids or proteins [33].

Figure 2 (bottom spectrum) shows a typical IR spectrum of a single fibroblast after 30 min of exposure to oxidative stress generated by $C_{60}(OH)_{19}(ONa)_{17}$ following the procedure explained above. The spectrum was acquired with the same parameters as for the control experiment. Compared to the non-exposed fibroblast, the most striking change is the appearance of a peak centered at 1740 $cm^{-1}$ (blue arrow). Nevertheless, the absolute increase of this peak could be due to a high number of lipid molecules and/or high lipid density in the cell. This could be especially the case when the aliphatic chains band (region 2995-2800 $cm^{-1}$, green arrow), which is connected to lipids, also increased. Therefore, we calculated the ratio between the C=O representative band and the lipids for N > 75 cells at three different time points T = 10, 20 and 30 min. Results are shown in Figure 3a. All values were normalized to control (1) where the cells were not subjected to any treatment. Control (2) and (3) were performed respectively in the presence of PS in the dark and after 20 min of illumination but without PS. Even though the distribution of the obtained values is relatively high, due to a strong heterogeneity among cells, the ratio between carbonyl ester groups in non-hydrogen bonded state and lipids, in each experimental group, were consistent and almost doubled after a 20 min OS exposure.

Specific protein-phosphorylation events have been previously demonstrated to occur during apoptosis and play an important role in the regulation of the programmed cell death mechanism

[34]. Hence, we also calculated the ratio between the asymmetric phosphate stretching region, 1280–1180 $cm^{-1}$, and the Amide I peak at 1710-1600 $cm^{-1}$ for N > 75 cells at three different time points T = 10, 20 and 30 min (Figure 3b).

To determine whether the differences in the means of the presented histograms are significant, we performed a two tails t-test comparing the control (1) with the 10, 20 and 30 min oxidative stress statistics. The data were expressed as means and standard errors. The obtained t values for for p = 0.1 or less were considered as significant. All our data fulfilled the imposed t-test conditions.

**Single cell mapping.** In order to localize characteristic spectral features at higher resolution we recorded an IR map of a single cell, by scanning the sample. The step size was 8 μm and the aperture was set to 7 μm, the diffraction-limited spatial resolution allowed a detailed mapping of a single cell with a size between ten and a few tens of a micrometer. Flat, well-spread cells were chosen by optical microscopy ensuring that the observed variations in intensity arose mostly from local concentration changes rather than from local thickness changes. Different distributions of the chemical functional groups are presented in Figure 4 and 5, for a non-treated fibroblast and for a fibroblast cell after a maximal exposure to photo-mediated OS (30 min / 500 μM PS in oxygenated PBS solution): (A) optical image of the cell, (B) distribution map of lipids computed from the integration of the aliphatic C-H stretching band area (2995-2800 $cm^{-1}$), (C) distribution map of proteins represented by the integration of the Amide I band area (1710-1600$cm^{-1}$), (D) ester distribution mapped by integration of the carbonyl ester group stretching band (1730-1760 $cm^{-1}$) and (E) asymmetric phosphate stretching represented by the 1280-1180

$cm^{-1}$ area. The protein distribution (C) for both, treated and non-treated cells exhibited a relatively homogenous distribution and high intensity at the cell center. This corresponded to the thickest part of the cell where the nucleus was also present, and in which a high protein density is found [35]. In contrast, the lipid distribution (B) was more spread, confirming that lipids are well distributed among the intracellular compartments, like the endoplasmic reticulum, the Golgi apparatus, the nuclear and cell membrane. No significant changes in either distribution were visible between the control and the treated cell, except that the treated cell was thicker and gave a stronger signal.

In order to normalize such thickness differences in cells, and detect relative changes in lipid peroxidation and protein phosphorylation from a non-treated to a treated cell (panels D and E in Figure 4), we also represented the peak ratios: 1730-1760 $cm^{-1}$ (C=O) over 2995-2800 $cm^{-1}$ (lipids) and 1280–1180 $cm^{-1}$ ($PO_2^-$) over 1710-1600 $cm^{-1}$ (Amide I). Both signatures were significantly enhanced upon ROS treatment (see Figure 5 panel D and E respectively), as it was already observed in single cell spectra (Figure 2, bottom).

**DISCUSSION AND CONCLUSION**

We have shown that $^1\Delta_g$ is generated within the timeframe of fullerol illumination (Figure 1b). This allowed us to conclude that the detected spectrum anomalies arising in the cells are largely due to the effect of $^1\Delta_g$. The most significant spectrum anomaly observed in cells exposed to OS was an increase of the peak around 1740 $cm^{-1}$, after 20 min of exposure to OS (Figure 3a). This was already observed by Holman et al. in dying fibroblasts, and attributed to the non-hydrogen-bonded ester carbonyl stretching mode in phospholipids [36]. Moreover, in previous studies this

peak increase was referred to an IR fingerprint of necrotic cells [16, 35]. In our case, it can be explained by the generation and accumulation of lipid peroxidation end products, known as Reactive Carbonyl Compound (RCC) such as e.g. malondialdehyde (MDA) [37] or acrolein [38]. Moreover, according to the chemical map of the cell in Figure 4 and 5 panel D, such increases are predominantly located in the cell periphery, distant from the nucleus (highlighted by a white dashed circle). Hence this pattern can be ascribed to the increase of oxidized lipids present in the membrane of dying cells. This feature, localized around the nucleus, is in excellent agreement with the study performed on necrotic cells by Dumas et al. [16].

On the other hand, the ratio between the peak partially associated with phosphorylated proteins (asymmetric phosphate stretching band, 1280–1180cm$^{-1}$) and the protein peak (Amide I, 1710-1600 cm$^{-1}$) integrated intensities started to increase earlier: after only 10 min of exposure to OS (as shown in Figure 3b). Specific protein-phosphorylation events are known to occur during apoptosis and also play an important role in the regulation of programmed cell death [39,40]. Cell mapping in Panels E (Figure 4 and 5) shows an increase in the phosphate contribution, spread over the whole cell, possibly indicating that cytoskeletal proteins were targeted during this apoptotic process. In summary, exposure to oxidative stress, and in particular $^1\Delta_g$, induces a cascade of lipid peroxidation and phosphorylation reactions within the observed cells. First, protein phosphorylation occurs within the cytoplasm and nucleus and later lipid phosphorylation of membrane structures. However, attributing this OS-induced phosphorylation to an apoptotic or necrotic reaction remains still open. It is very likely that a combination of both pathways exists.

Concerning the distribution in the value obtained in our statistical sampling, it is worth noting that the cells studied after exposure to oxidative stress, might have been those which better resisted the photo-mediated action. Considering the experimental procedure, those cells with more damage had a higher likelihood to detach from the surface and were then washed away during the multiple rinsing steps. Therefore, they were not considered in this study, which compromised the statistics. In conclusion, we successfully used FTIRM to detect small OS-mediated biochemical changes in cells. Especially, lipid peroxidation and protein phosphorylation have been identified as OS fingerprint. These features were characterized by an increase of the ester (1740 $cm^{-1}$) and phosphate asymmetric stretching (1240 $cm^{-1}$) related peaks respectively.

**ACKNOWLEDGEMENTS**

The authors are also particularly thankful to Randy Smith for his technical assistance and Dr. Titusz Feher for his constructive discussions. The NSLS is supported by the United States Department of Energy under contract DE-AC02-98CH10886. These studies were also partially supported by the Swiss National Science Foundation, project No. 205320 – 112164, "Biomolecules under stress: ESR *in vitro* study" (A.S. and L.F.).

**REFERENCES**

1. 1] T. Finkel, N.J. Holbrook. Oxidants, oxidative stress and the biology of ageing. Nature, 408 (2000) 239–247.

2. 1] A.P. Castano, P.Mroz, M.R. Hamblin, Photodynamic therapy and anti-tumour immunity, Nature Cancer Rev. 6 (2006) 535.

3. 1] T.J. Dougherty, An update on photodynamic therapy applications, J. Clin. Laser. Med. Surg. 20 (2002) 3–7.

4. 1] K. Scharffetter-Kochanek, P. Brenneisen, J. Wenk, G. Herrmann, W.J. Ma, L. Kuhr, C. Meewes, M. Wlaschek, Photoaging of the skin from phenotype to mechanisms Exp. Gerontol. 35 (2000) 307-316.

5. 1] E. Mariani, M.C. Polidori, A. Cherubini P. Mecocci. Oxidative stress in brain aging, neurodegenerative and vascular diseases: An overview. J. Chromat. B. 825 (2005) 65–75.

6. 1] S. Beatty, H.H. Koh, D. Henson, M. Boulton, The role of oxidative stress in the pathogenesis of age-related macular degeneration Survey. of Ophtalmol. 45 (2000) 115-134

7. 1] A. Dewilde, C. Pellieux, S. Hajjam, P. Wattre, C. Pierlot, D. Hober, J-M Aubry, Virucidal activity of pure singlet oxygen generated by thermolysis of a water-soluble naphthalene endoperoxide, J. Photochem. Photobiol. B. 26 (1996) 23-29.

8. 1] R.W. Redmond, I.E. Kochevar, Spacially resolved cellular responses to singlet oxygen, Photochem. Photobiol. 82 (2006) 1178-1186.

9. 1] I.E. Kochevar, M.C. Lynch, S. Zhuang, C.R. Lambert, Singlet Oxygen, but not Oxidizing Radicals, Induces Apoptosis in HL-60 Cells, Photochem. and Photobiol. 72 (2002) 548–553.

10. 1] Y. Yamakoshi, N.Umezawa, A. Ryu, K. Arakane, N. Miyata, Y. Goda, T. Masumizu T. Nagano, Active oxygen species generated from photoexcited fullerene ($C_{60}$) as potential medicines: $O_2^{-}$* versus $^1O_2$, J. Am. Chem. Soc. 125 (2003) 12803–12809.

11. 1] A.R. Badireddy, E.M. Hotze, S. Chellam, P. Alvarez, M.R. Wiesner. Inactivation of Bacteriophages via Photosensitization of Fullerol Nanoparticles. Environ. Sci. Technol. 41 (2007) 6627-6632.

12. 1] B. Vileno, P.R. Marcoux, M. Lekka, A. Sienkiewicz, T. Feher, L. Forró. Spectroscopic and photophysical properties of a highly derivatized C60 fullerol. Adv. Func. Mater., 16 (2006) 120–128.

13. 1] A. Sienkiewicz, B. Vileno, K. Pierzchała, M. Czuba, P.R. Marcoux, A. Graczyk, P.G Fajer, L. Forró, "Oxidative stress-mediated protein conformation changes: ESR study of spin-labelled staphylococcal nuclease, J. Phys. Condens. Mat. 19 (2007) 285201.

14. 1] L.M. Miller, R.J. Smith, Synchrotrons versus globars, point-detectors versus focal plane arrays: selecting the best source and detector for specific infrared microspectroscopy and imaging applications, Vib. Spectrosc. 38 (2005) 237–240.

15. 1] L.M. Miller, P. Dumas, Chemical imaging of biological tissue with synchrotron infrared light, Biochim. Biophys. Acta. 1758 (2006) 846–857.

16. 1] P. Dumas and L.M. Miller. The use of synchrotron infrared microspectroscopy in biological and biomedical investigations, Vib. Spectrosc, 32 (2003) 3–21.

17. 1] L. Y. Chiang, R. B. Upasani, J. W. Swirczewski, US Patent 5 177 248, 1993.

18. 1] Z. Markovic, V. Trajkovic, Biomedical potential of the reactive oxygen species generation and quenching by fullerenes ($C_{60}$), Biomaterials. 29 (2008) 3561–3573.

19. 1] Y. Lion, M. Delmelle, A. van de Vorst, New method of detecting singlet oxygen production, Nature. 263 (1976) 442–443.

20. 1] T. Ando, T. Yoshikawa, T. Tanigawa, M. Kohno, N. Yoshida, M. Kondo, Quantification of singlet oxygen from hematoporphyrin derivative by electron spin resonance, Life Sci. 61 (1997) 1953–1959.

21. 1] P. Steiner, J. C. F. Sarria, L. Glauser, S. Magnin, S. Catsicas, H. Hirling, Modulation of receptor cycling by neuron-enriched endosomal protein of 21 KD, J. Cell Biol. 157 (2002) 1197 1209.

22. 1] J. Ramesh, A. Salman, Z. Hammody, B. Cohen, J. Gopas, N. Grossman, S. Mordechai, FTIR microscopic studies on normal and h-ras oncogene transfected cultured mouse fibroblasts, Eur. Biophys. J. 30 (2001) 250–255.

23. 1]M. A. Cohenford, B. Rigas, Cytologically normal cells from neoplastic cervical samples display extensive structural abnormalities on IR spectroscopy: Implications for tumor biology, Proc. Natl. Acad. Sci. 95 (1998) 15327–15332.

24. 1] K.Z. Liu, H. H. Mantsch, Apoptosis-induced structural changes in leukemia cells identified by IR spectroscopy, J. Molec. Struct. 565 (2001) 299–304.

25. 1] L. M. Miller, G. D. Smith, G.L. Carr, Synchrotron-based biological microspectroscopy: From the mid-infrared through the far-infrared regimes, J. Biol. Phys. 29 (2003) 219–230.

26. 1] M.C. Martin, N.M. Tsvetkova, J.H. Crowe, W.R. McKinney, Negligible sample heating from synchrotron infrared beam, Appl. Spectros. 55 (2001) 111–113.

27. 1] B. Stuart. Biological applications of Infrared Spectroscopy, D.J. Ando Ed., John Wiley & sons NY, 1997.

28. 1] F. Siebert. Infrared-spectroscopy applied to biochemical and biological problems, Meth. Enzym, 246 (1995) 501–526.

29. 1] F. Severcan, N. Toyran, N. Kaptan, B. Turan, Fourier transform infrared study of the effect of diabetes on rat liver and heart tissues in the C-H region, Talanta 53 (2000) 55–59..

30. 1] J. Kneipp, P. Lasch, E. Baldauf, M. Beekes, D. Naumann, Detection of pathological molecular alterations in scrapie-infected hamster brain by Fourier transform infrared (FT-IR) spectroscopy, Biochim. Biophys. Acta. 1501 (2000)189-199.

31. 1] A. Barth. Infrared spectroscopy of proteins. Biochimica et Biophysica Acta 1767:1073–1101, 2007.

32. 1] R. Schweitzer-Stenner, Advances in vibrational spectroscopy as a sensitive probe of peptide and protein structure A critical review, Vib. Spectrosc. 42 (2006) 98–117.

33. 1] P. Dumas, L.M. Miller, Biological and Biomedical Applications of Synchrotron Infrared Microspectroscopy, J. Biol. Phys. 29 (2003) 201–218.

34. 1] B.T. Gjertsen, S.O. Doskeland, Protein-phosphorylation in apoptosis, Biochim. Biophys. Acta- Molec. Cell Res. 1269 (1995) 187–199.

35. 1] N. Jamin, P. Dumas, J. Moncuit, W.H. Fridman, J.L. Teillaud, G.L. Carr, G.P. Williams, Highly resolved chemical imaging of living cells by using synchrotron infrared microspectrometry, Proc. Natl. Acad. Sci. 95 (1998) 4837–4840.

36. 1] H.N. Holman, M.C. Martin, E.A. Blakely, K. Bjornstad, W.R. McKinney. IR spectroscopic characteristics of cell cycle and cell death probed by synchrotron radiation based Fourier transform IR spectromicroscopy, Biopolymers. 57 (2000) 329–335.

37. 1] D. Del Rio, A.J. Stewart, N. Pelligrini, A review of recent studies of malondialdehyde as toxic molecule and biological marker of oxidative stress. Nutr. Metab Cardiovas. 15 (2005) 316.

38. 1] K. Uchida, M. Kanematsu, Y. Morimitsu, T. Osawa, N. Noguchi, E. Niki, Acrolein Is a Product of Lipid Peroxidation Reaction. J. Biol. Chem. 273 (1998) 16058.

39. 1] B.T. Gjertsen, S.O. Doskeland. Protein phosphorylation in apoptosis, Biochim. Biophys. Acta. 1269 (1995) 187-199.

40. 1] P.K. Davis, G.V.W. Johnson. Energy metabolism and protein phosphorylation during apoptosis: A phosphorylation study of tau and high-molecular-weight tau in differentiated PC12 cells, Biochem. J. 340 (1999) 51–58.

**FIGURE CAPTIONS**

**Figure 1:** (a) Reactive mechanism of TEMPOL generation (paramagnetic) resulting from TMP-OH (diamagnetic) scavenging of $^1\Delta_g$. (b) Evolution of the EPR signal of TEMPOL at different illumination times in the process of $^1\Delta_g$-photosensitization in oxygen-saturated 500 μM of $C_{60}(OH)_{19}(ONa)_{17}$ supplemented with 50 mM of TMP-OH.

**Figure 2:** Infrared spectra of dried single monkey fibroblasts for: (top) a non-treated cell (ctrl) and (bottom) a cell exposed to photo-mediated OS for 30 min in an oxygenated 500 μM fullerol in PBS solution. The aperture was set to 10 x 10 $\mu m^2$, the instrumental resolution to 4 $cm^{-1}$, and 256 spectra were accumulated. A baseline was subtracted for both spectra.

**Figure 3:** Histograms of the integrated area ratio between (a) the ester carbonyl stretching mode (1760-1730 $cm^{-1}$ region) and the aliphatic C-H stretch region (2995-2800 $cm^{-1}$ region) and (b) between the phosphorylated protein peak area (asymmetric phosphate stretching band, 1280–1180 $cm^{-1}$) and the protein peak area (Amide I, 1710-1600 $cm^{-1}$). Controls were the following: (1) no treatment. (2) 20 min in the presence of fullerols in the dark. (3) 20 min illumination in PBS without PS. OS exposure: cells were illuminated in the presence of 500 μM of $C_{60}(OH)_{19}(ONa)_{17}$ in PBS saturated with oxygen, for different exposure times (10, 20 and 30 min). All the values were normalized by the control (1). Average values were calculated assuming a Gaussian distribution of our experimental values. The error was taken as the full width at half maximum (FWHM) of the Gaussian.

**Figure 4:** Single cell mapping of the functional group distribution for a non-treated (CTRL) fibroblast (top row) and exposed for 30 min to OS (bottom row). (A) Optical image of a single cell. (B) Lipid distribution map associated to the aliphatic C-H stretch band (2995-2800 $cm^{-1}$) (C) Protein distribution map resulting from the Amide I peak integration (1710-1600$cm^{-1}$) (D) Asymmetric phosphate stretching distribution (1280-1180$cm^{-1}$). (E) Ester distribution map illustrated by carbonyl ester group stretch (1730-1760 $cm^{-1}$). The spectra were recorded with an aperture of 8 x 8 $\mu m^2$ with a step size of 7 μm, a resolution of 4 $cm^{-1}$. 256 scans were accumulated. The scale bar on A represents 8 μm. The concentrations of each component scale from blue (0) to red (max).

**Figure 5:** Single cell mapping of the functional group distribution for a non-treated (CTRL) fibroblast (top row) and exposed for 30 min to OS (bottom row). (A) Optical image of a single cell. (D) Ratio of the bands 1730-1760 $cm^{-1}$ (C=O) and 2995-2800 $cm^{-1}$ (lipids). (E) Ratio of the bands 1280-1180$cm^{-1}$ ($PO_2^-$) and 1710-1600$cm^{-1}$ (Protein). The spectra were recorded with an aperture of 8 x 8 $\mu m^2$ with a step size of 7 μm, a resolution of 4 $cm^{-1}$. 256 scans were accumulated. The scale bar on A represents 8 μm. The concentrations of each component scale from blue (0) to red (max), white corresponds to values out of range, when the ratio is diverging (obtained for a very low absorbance value *i.e.* when the probed area is empty).

Figure 1

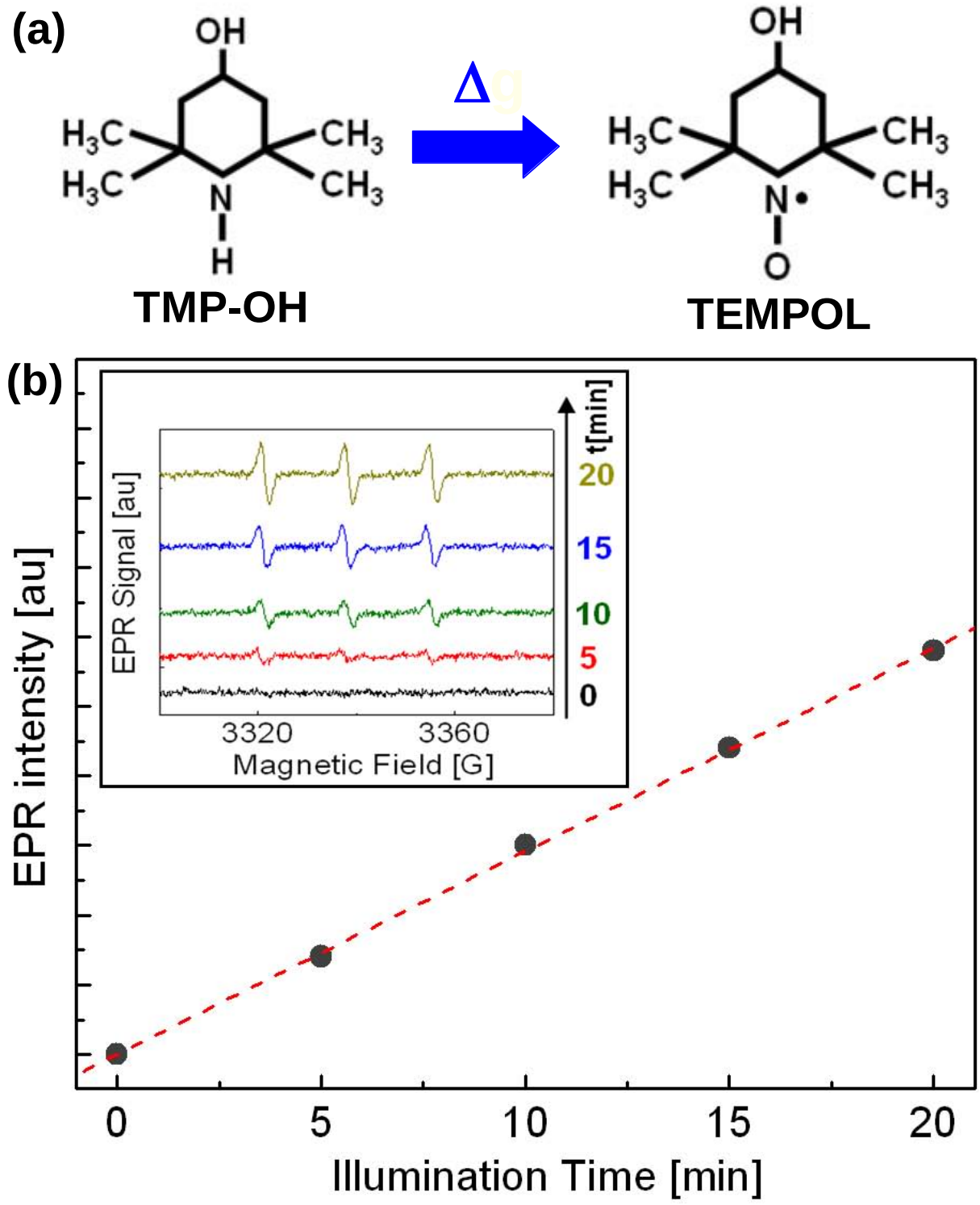

Figure 2

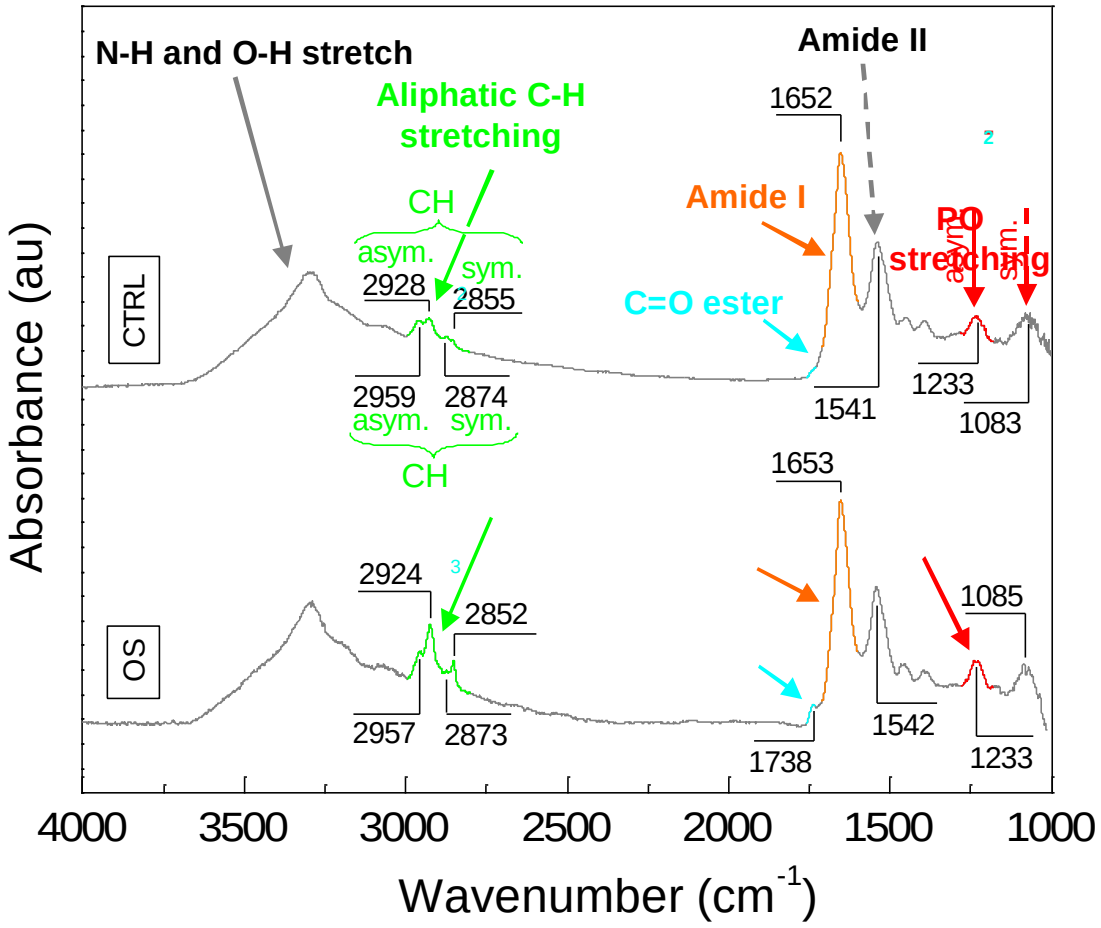

Figure 3

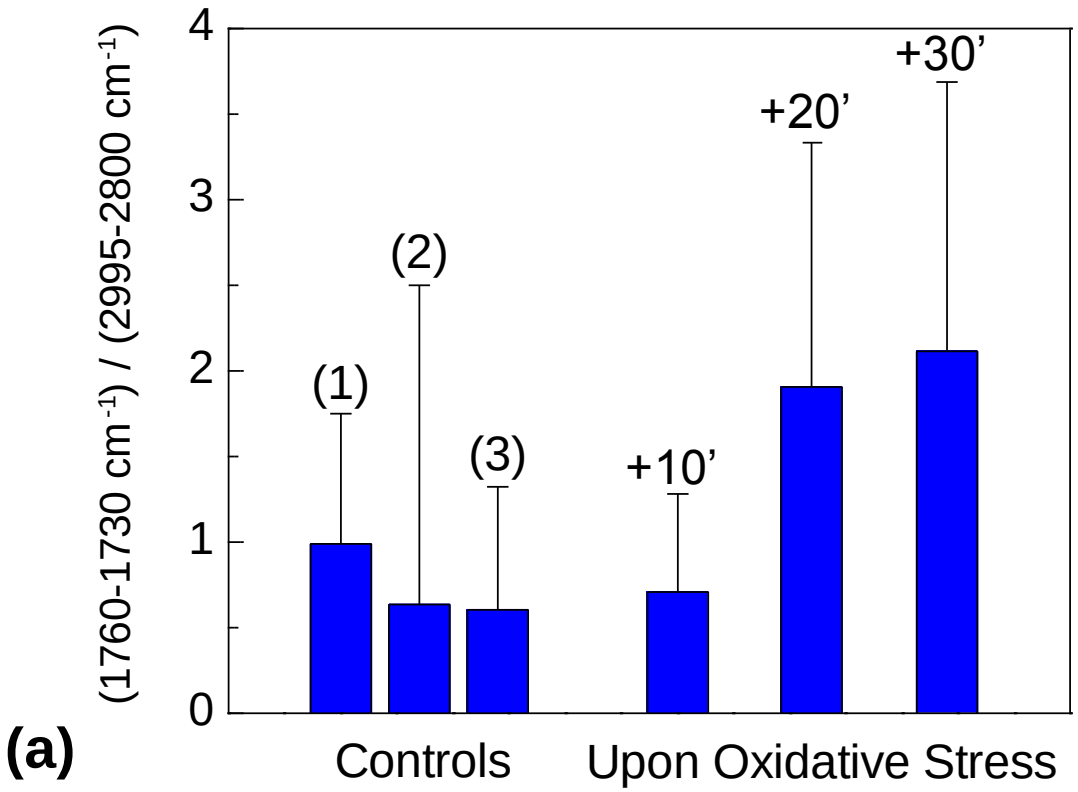


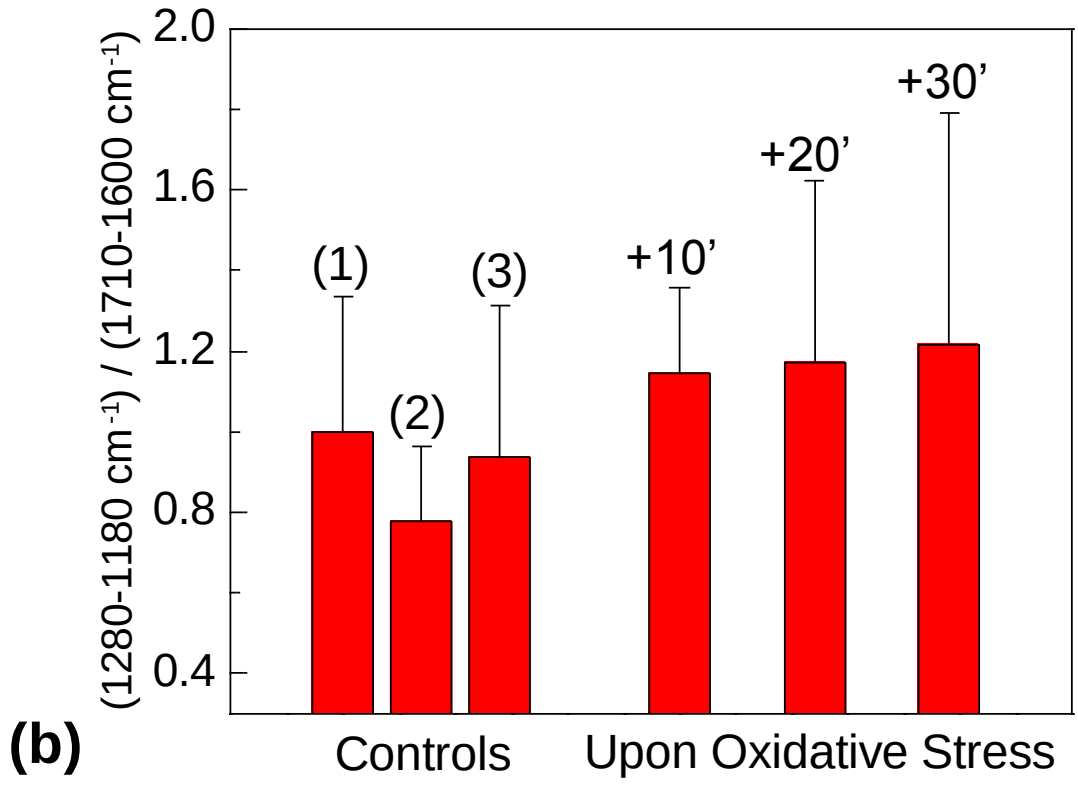

Figure 4

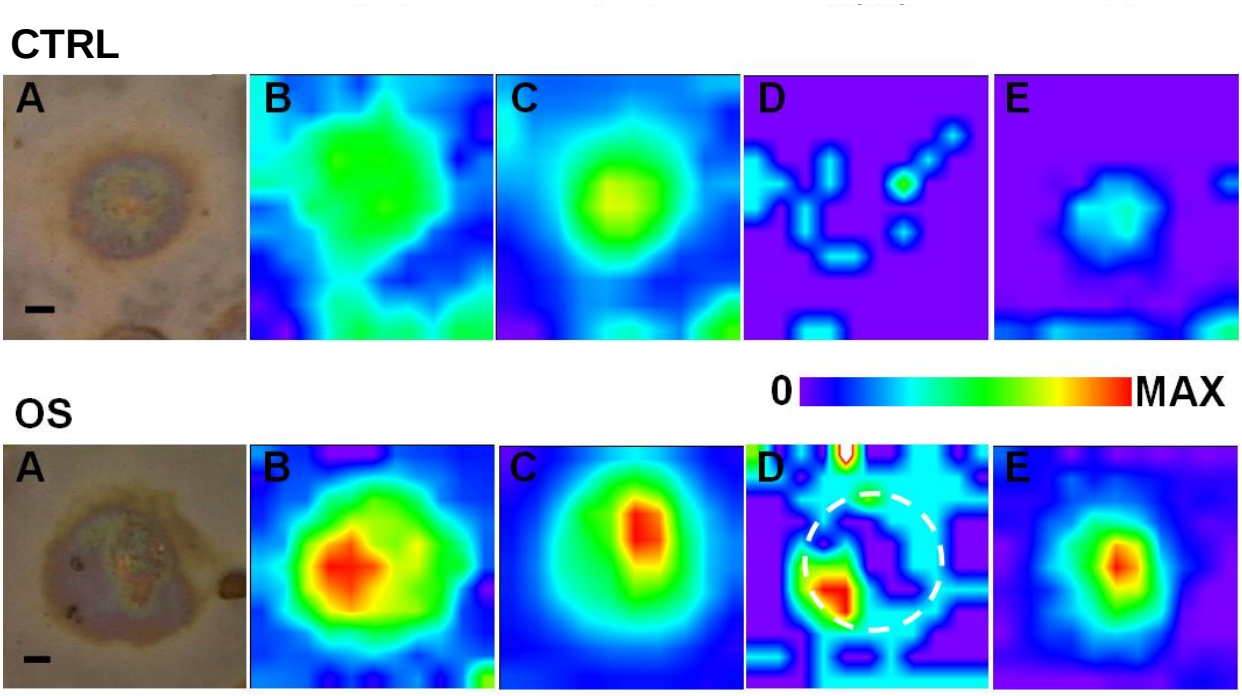

Figure 5